

OPEN

# Solution-Based Synthesis of Few-Layer $WS_2$ Large Area Continuous Films for Electronic Applications

Omar A. Abbas<sup>1,5</sup>, Ioannis Zeimpekis<sup>1,5</sup>, He Wang<sup>2</sup>, Adam H. Lewis<sup>1</sup>, Neil P. Sessions<sup>1</sup>, Martin Ebert<sup>3</sup>, Nikolaos Aspiotis<sup>1</sup>, Chung-Che Huang<sup>1</sup>, Daniel Hewak<sup>1</sup>, Sakellaris Mailis<sup>1,4</sup> & Pier Sazio<sup>1\*</sup>

Unlike  $MoS_2$  ultra-thin films, where solution-based single source precursor synthesis for electronic applications has been widely studied, growing uniform and large area few-layer  $WS_2$  films using this approach has been more challenging. Here, we report a method for growth of few-layer  $WS_2$  that results in continuous and uniform films over centimetre scale. The method is based on the thermolysis of spin coated ammonium tetrathiotungstate ( $(NH_4)_2WS_4$ ) films by two-step high temperature annealing without additional sulphurization. This facile and scalable growth method solves previously encountered film uniformity issues. Atomic force microscopy (AFM) and transmission electron microscopy (TEM) were used to confirm the few-layer nature of  $WS_2$  films. Raman and X-Ray photoelectron spectroscopy (XPS) revealed that the synthesized few-layer  $WS_2$  films are highly crystalline and stoichiometric. Finally,  $WS_2$  films as-deposited on  $SiO_2/Si$  substrates were used to fabricate a backgated Field Effect Transistor (FET) device for the first time using this precursor to demonstrate the electronic functionality of the material and further validate the method.

2D transition metal dichalcogenides (TMD) have emerged as promising low dimensional semiconductor materials<sup>1</sup> due to their exceptional electrical, optical and mechanical properties<sup>2</sup>. Among the TMD family,  $MoS_2$  has been the first and most investigated member because of its excellent properties such as thickness dependent indirect to direct bandgap transition<sup>3,4</sup>, valley Hall effect<sup>5</sup>, high carrier mobility and on-off ratio<sup>6</sup> that makes it suitable for a wide range of electronic applications. A significant number of scientific reports have addressed the synthesis routes of  $MoS_2$ . The production methods reported in the literature include mechanical<sup>6</sup> or liquid exfoliation<sup>7</sup> as well as conventional atomic layer deposition (ALD)<sup>8</sup> and chemical vapour deposition (CVD)<sup>9</sup>. These approaches however are still far from being commercially viable due to low yield and/or high costs.

Two significant factors that identify a successful route to commercialization of a material are its compatibility with existing fabrication methods and cost effectiveness. Solution-based synthesis is compatible with existing nanofabrication processes, is scalable at low cost and has already been shown to produce high quality  $MoS_2$  films using a single source precursor such as ammonium tetrathiomolybdate  $(NH_4)_2MoS_4$  through thermal decomposition for electronic devices applications<sup>10</sup>. Therefore, several groups have developed approaches for large area solution-based  $MoS_2$  synthesis via two-step thermolysis of  $(NH_4)_2MoS_4$  films coated in different ways such as dip, roll to roll and spin coating<sup>11–18</sup>. Spin coating of  $(NH_4)_2MoS_4$  solution in particular is highly preferable among other coating techniques due to its integration with current semiconductor technology and its ability to control the initial precursor film thickness through spinning speed as well as precursor solution concentration<sup>13,17</sup>. The main obstacle hindering this coating technique is the low wettability of precursor solutions that utilize common solvents such as dimethylformamide (DMF) and n-methylpyrrolidone (NMP), with commonly used substrates like  $SiO_2/Si$  or sapphire. This leads to nonuniform precursor film formation associated with a high density of defects and de-wetted areas after spin coating. To overcome this issue, researchers developed different organic-precursor solution systems for spin coating to enhance the uniformity and controllability of the initial precursor film over large area and eliminate surface defects. These organic-precursor solutions systems are: DMF,

<sup>1</sup>Optoelectronics Research Centre, University of Southampton, Southampton, SO17 1BJ, United Kingdom. <sup>2</sup>National Centre for Advanced Tribology, University of Southampton, Southampton, SO17 1BJ, United Kingdom. <sup>3</sup>School of Electronics and Computer Science, University of Southampton, Southampton, SO17 1BJ, United Kingdom. <sup>4</sup>Present address: Skolkovo Institute of Science and Technology Novaya St., 100, Skolkovo, 143025, Russian Federation.

<sup>5</sup>These authors contributed equally: Omar A. Abbas and Ioannis Zeimpekis. \*email: [pjas@soton.ac.uk](mailto:pjas@soton.ac.uk)

n-butylamine and 2-aminoethanol<sup>13</sup>; ethylenediaminetetraacetic acid (EDTA) and dimethylsulfoxide (DMSO)<sup>16</sup>; and linear poly (ethylenimine), DMF and 2-aminoethanol<sup>17</sup>.

Similarly, WS<sub>2</sub> is an important TMD material which shows comparable characteristics to MoS<sub>2</sub> but can also offers higher photoluminescence (PL) efficiency, better electrical performance and ambipolar field effect behaviour<sup>19–21</sup>. Although WS<sub>2</sub> has growth methods similar to MoS<sub>2</sub> such as sulphurization of tungsten metal<sup>22</sup> or tungsten oxides<sup>23</sup>, growth of large area and uniform WS<sub>2</sub> ultra-thin films for electronic applications via thermal decomposition of ammonium tetrathiotungstate (NH<sub>4</sub>)<sub>2</sub>WS<sub>4</sub> salt has not been demonstrated successfully. This is due to the difficulty that is associated with the formation of a thin uniform (NH<sub>4</sub>)<sub>2</sub>WS<sub>4</sub> precursor layer as this salt has poor solubility in most of the common solvents as compared with (NH<sub>4</sub>)<sub>2</sub>MoS<sub>4</sub><sup>24</sup>. Usage of these solvents in solution-based single source precursor deposition of WS<sub>2</sub> has however been demonstrated for applications that do not require highly continuous WS<sub>2</sub> films, such as surface enhancement Raman scattering (SERS) and creating a carrier injector layer for optoelectronic devices<sup>25,26</sup>. Another issue in solution-based single source precursor synthesis by thermal decomposition occurs when the second annealing step is relatively high (<800 °C). In this case, sulphur from (NH<sub>4</sub>)<sub>2</sub>MoS<sub>4</sub> and (NH<sub>4</sub>)<sub>2</sub>WS<sub>4</sub> films evaporates readily and needs to be substituted by adding sulphur in the inert gas flow to preserve the stoichiometry and the quality of the MoS<sub>2</sub> and WS<sub>2</sub> films<sup>11,13,25,26</sup>.

Generally, there are three factors that need to be optimized to create a defect-free film from a liquid precursor by spin coating; the wettability of the precursor solution with the substrate, the solubility of precursor in the solvent system and the viscosity of the solution. Wettability can be significantly improved by oxygen plasma treatment of the substrate which promotes the hydrophilicity of the surface<sup>13</sup>. Choosing a solvent capable of achieving high solubility of the precursor helps to eliminate clusters and striation formation due to surface tension. Viscosity can be controlled by the choice of the solvents system and the concentration of the precursor, which affects the coverage of the film over the substrate and the final precursor film thickness<sup>13,17</sup>.

We have therefore optimized all three parameters to create uniform large area ultra-thin WS<sub>2</sub> layers via a two-step thermal decomposition of (NH<sub>4</sub>)<sub>2</sub>WS<sub>4</sub> spun-coated precursor solutions. A refined solvent recipe was formulated to improve the wettability and uniformity of the precursor film on the substrate. Additionally, by processing our samples in a “facing pair” manner during the high temperature second annealing step, the composition/stoichiometry of the films was preserved, thus eliminating the need for additional sulphurization. Optical microscopy was used to assess the uniformity and continuity of the precursor films while AFM and TEM evaluated the resulting WS<sub>2</sub> film thickness and morphology. Raman spectroscopy supported the AFM and TEM results to identify the few-layer nature of the films and showed the effect of temperature on the crystallinity of the film. XPS spectroscopy revealed the stoichiometry of WS<sub>2</sub> films when grown on different substrates. Finally, an FET device was fabricated using as-deposited WS<sub>2</sub> film to further elucidate the potential electronic applications of these films.

## Results and Discussion

Electronic devices such as FETs require continuous and uniform films for the device layer to guarantee high electrical performance. In solution-based synthesis of semiconducting WS<sub>2</sub> films, the main defects are pinholes and de-wetted areas over the substrate that occur in the precursor deposition step. In this work we have tackled these issues by refining the solvents system for the (NH<sub>4</sub>)<sub>2</sub>WS<sub>4</sub>.

There are simple solutions for wettability but because (NH<sub>4</sub>)<sub>2</sub>WS<sub>4</sub> is weakly coordinated with most of the solvents<sup>24</sup>, the key challenge in making a solution-based uniform ultra-thin WS<sub>2</sub> film is formulating a solution recipe that results in a high solubility of the precursor with the optimum viscosity. Based on this, we chose the most promising solvents reported previously for spin coating, namely (DMF)<sup>27</sup>, ethylene glycol<sup>26</sup>, (NMP)<sup>12</sup> to investigate which one has the maximum solvation and coverage over the substrate. Preparation of the substrates and precursor solutions for spin coating is described in Materials and Methods.

Figure 1(A–C), shows the spin-coated precursor films where (NH<sub>4</sub>)<sub>2</sub>WS<sub>4</sub> is dissolved in DMF, ethylene glycol and NMP solvents respectively (100 mM solution concentration), at 6000 rpm spinning speed. Unfortunately, none of the solvents successfully formed continuous and uniform (NH<sub>4</sub>)<sub>2</sub>WS<sub>4</sub> films. The high concentration and therefore viscosity of the solutions should have facilitated the continuous film formation, opposite to what we observed here. Moreover, the de-wetted regions were significantly enlarged at 9000 rpm which was the peak of the spin coating speed (see Fig. S1). DMF was promising in terms of forming continuous precursor films with excellent surface coverage at 3000 and 6000 rpm speeds. Unfortunately, we identified high density of clusters that probably consist of insoluble WS<sub>4</sub><sup>−2</sup> anions. Ethylene glycol based film exhibited lower density of clusters as compared to DMF at 3000 rpm (see Fig. S1) but had more de-wetted regions, with the wettability deteriorating at moderate and high spin coating speeds, thus preventing the formation of a thin uniform layer. Unlike the previous solvents, NMP showed some more solvation without forming clusters at all spin coating speeds, indicating a better solvation of (NH<sub>4</sub>)<sub>2</sub>WS<sub>4</sub> by NMP compared to DMF and ethylene glycol solvents. However, the high density of random pinholes assigned to insufficient wetting of the solution with the substrate.

It has been reported before that amine-based solvents could be linked with WS<sub>4</sub><sup>−2</sup> anions via hydrogen bonds leading to form a stable solution<sup>28,29</sup>. Additionally, it has been shown that n-butylamine and 2-aminoethanol solvents can stabilize the (NH<sub>4</sub>)<sub>2</sub>MoS<sub>4</sub> and bind the solution to create uniform MoS<sub>2</sub> precursor films by spin coating<sup>13</sup>. However, this (NH<sub>4</sub>)<sub>2</sub>MoS<sub>4</sub> solvents recipe contains DMF rather than NMP which leads to non-uniform WS<sub>2</sub> precursor layer formation when it was used for (NH<sub>4</sub>)<sub>2</sub>WS<sub>4</sub> (see Fig. S2). Based on these facts, we reformulated the recipe of NMP by adding the solvents butylamine and 2-aminoethanol (see Materials and Methods). Moreover, to ensure good coverage and uniformity of the spin-coated precursor layer, we started with high concentration solution (100 mM), as is evident from Fig. 1(D) there was a significant improvement of the uniformity without any obvious de-wetted regions over a large area. The few apparent micron-sized defects originated from particles on the substrate. However, further reduction in precursor solution concentration was needed in order to achieve WS<sub>2</sub> films with minimum thickness. Therefore, we used the same solvents recipe with the threshold concentration (35 mM) of

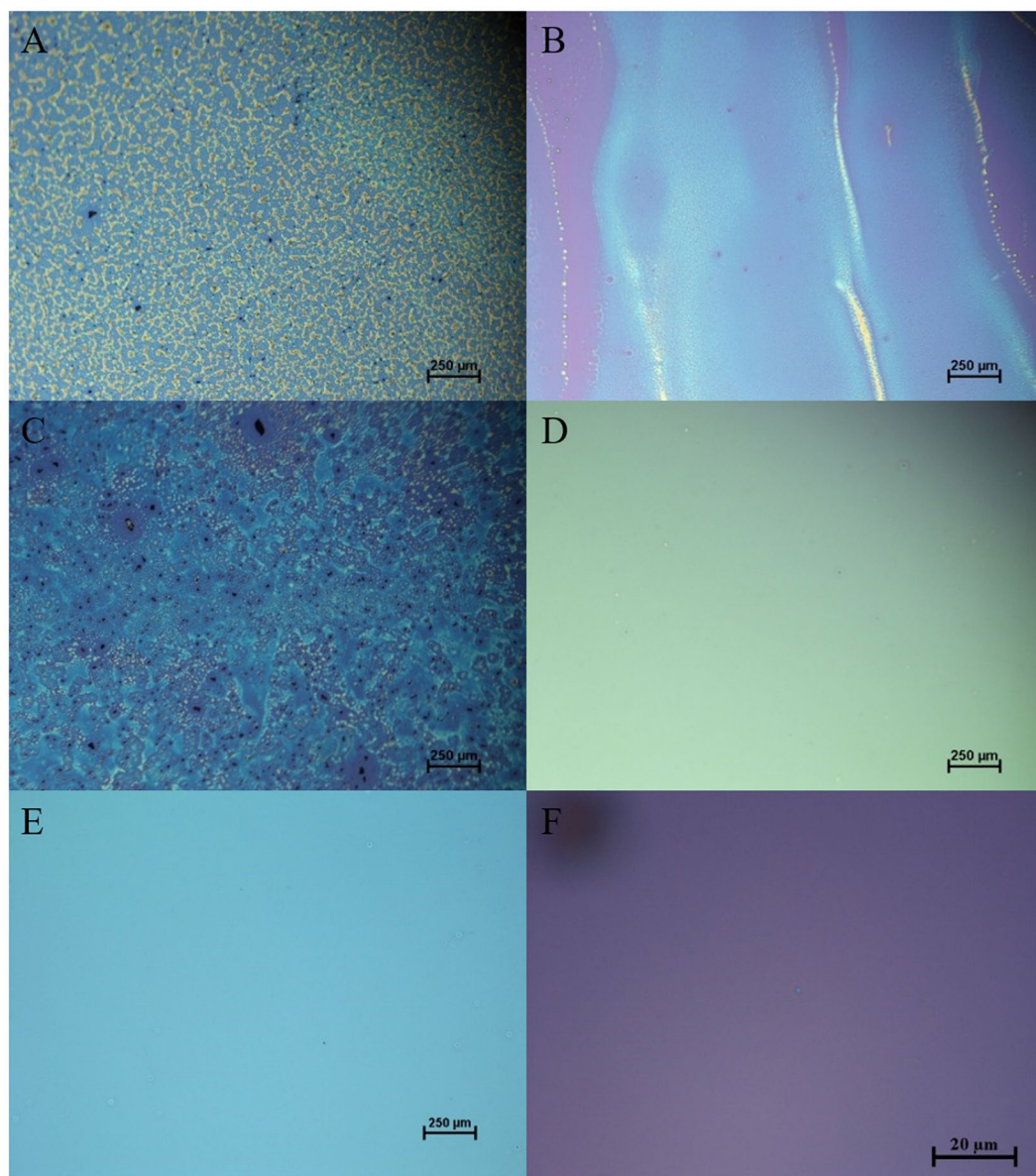


**Figure 1.** Optical microscope images of spin-coated precursor films prepared by dissolving 100 mM of  $(\text{NH}_4)_2\text{WS}_4$  in: (A) dimethylformamide (DMF), (B) ethylene glycol, (C) n-methylpyrrolidone (NMP) and (D) solvent system contains (3 mL NMP/2 mL n-butylamine/1 mL 2-aminoethanol of 6 mL total volume). (E,F) are optical microscope images of spin-coated precursor films prepared by dissolving 35 mM of  $(\text{NH}_4)_2\text{WS}_4$  in (3 mL NMP/2 mL n-butylamine/1 mL 2-aminoethanol of 6 mL total volume). All the solutions are spin coated at 6000 rpm for 1 min and prebaked at 140 °C for 1 min. Note that (A–E) images were taken using 5X objective while (F) image was taken using 100X objective.

$(\text{NH}_4)_2\text{WS}_4$  that can produce large area and uniform precursor films as shown in Fig. 1(E–F) respectively. At lower concentrations than this (e.g. 10 or 20 mM), the density of  $\text{WS}_4$  anions in the solution were very low leading to formation of isolated micron-sized islands rather than a continuous film (see Fig. S3).

After the second annealing step of  $\text{WS}_2$  films grown on  $\text{SiO}_2/\text{Si}$  and sapphire substrates (with 35 mM precursor concentration), the topography and thickness of these samples were assessed by atomic force microscopy (AFM). The average thickness of the films for an area of edges was  $6.5 \pm 0.68$  nm (0.68 nm is the root mean square roughness  $R_q$  of the film) for the  $\text{SiO}_2/\text{Si}$  substrate and  $6 \pm 0.1$  nm (0.1 nm is the root mean square roughness  $R_q$  of the film) for the sapphire as shown in Fig. 2. The higher roughness of the film grown on the  $\text{SiO}_2/\text{Si}$  substrate is attributed to the amorphous nature of the substrate and to the increased surface roughness caused by the relatively long time exposed to oxygen plasma. As AFM measurements were taken at the edge of  $\text{WS}_2$  films where they are prone to edge effects from the spinning process, therefore, these AFM results represent the maximum thickness of  $\text{WS}_2$  films. Additionally, the AFM images confirm the continuity of the  $\text{WS}_2$  films with small grains that appear due to the nano-size crystals formed at the  $\text{WS}_2$  uniform film.

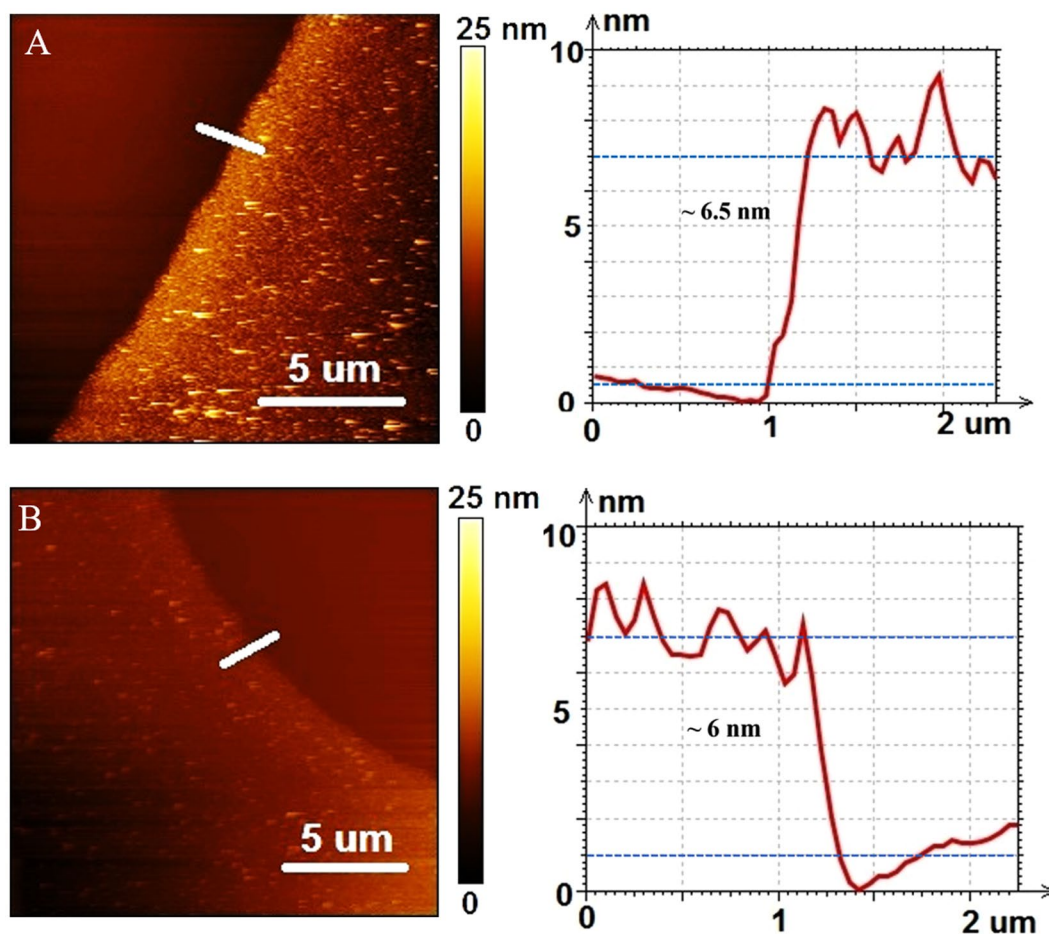


**Figure 2.** Atomic force microscopy (AFM) images of WS<sub>2</sub> films grown on (A) SiO<sub>2</sub>/Si (B) sapphire.

To evaluate the structure of the WS<sub>2</sub> films at the central area of the samples, TEM was conducted for the film grown on a sapphire substrate. Figure 3 shows a TEM image of the WS<sub>2</sub> film demonstrating a highly ordered layered structure. It is apparent from Fig. 3, the film is uniform and constituted by areas of 2 and 3 layers. The TEM image indicates that the single layer thickness of the WS<sub>2</sub> film is 0.65 nm, in agreement with previously reported WS<sub>2</sub> monolayer thickness<sup>23</sup>. At the bottom right of Fig. 3 and also in Fig. S4 arranged columns of atoms are clearly visible.

Raman spectroscopy with a 532 nm excitation wavelength was performed to characterize the WS<sub>2</sub> films on both SiO<sub>2</sub>/Si and sapphire substrates for each of the two-annealing steps (500 °C and 1000 °C). The consequence of using a 532 nm pump laser for Raman spectroscopy is an enrichment of the Raman spectra with second order peaks<sup>30</sup>. Multi-peak Lorentzian fitting is applied to deconvolute these peaks which helps to reveal any crystallinity changes between the two-annealing steps and to estimate the thickness of the films. As shown in Fig. 4 after the 1000 °C anneal, the Raman spectra intensity at the centre of the samples were enhanced by X2 for the SiO<sub>2</sub>/Si and X4 for the sample grown on sapphire. Moreover, all peaks become narrower after the second annealing step. The most dramatic change was with the peak labelled LA (M)-TA(M)<sup>31</sup> where its FWHM was reduced from 63.4 cm<sup>-1</sup> in the first annealing step to 24.4 cm<sup>-1</sup> in the second annealing step for SiO<sub>2</sub>/Si and from 51 cm<sup>-1</sup> to 28 cm<sup>-1</sup> for sapphire. Additional peaks that correspond to 2LA (K) mode<sup>32</sup> are also apparent at 385.2 cm<sup>-1</sup> and 387.7 cm<sup>-1</sup> for SiO<sub>2</sub>/Si and sapphire respectively, which did not exist after the first annealing step. The intensity enhancement in the Raman spectra, the reduction in full width half maximum (FWHM) of all Raman peaks as well as the prominence of additional second order peak (2LA (K)) highlight the significance of the second annealing step at high temperature (1000 °C) to promote the crystallinity of the WS<sub>2</sub> films.

Furthermore, at 500 °C the intensity of the in-plane E<sub>2g</sub><sup>1</sup> (Γ) dominated the longitudinal 2LA (M) mode whereas at the 1000 °C the 2LA (M) peaks increased in intensity which almost overwhelmed the E<sub>2g</sub><sup>1</sup> (Γ) mode for all substrates. In contrast, the out-of-plane peak A<sub>1g</sub><sup>1</sup> (Γ) decreased in intensity at the higher temperature. Consequently, the 2LA (M)/A<sub>1g</sub><sup>1</sup> (Γ) intensity ratio increased dramatically from 0.685 at 500 °C to 2.64 at 1000 °C for the SiO<sub>2</sub>/Si and from 0.285 to 2.26 for the sapphire. Moreover, the Raman peak difference between the in-plane mode E<sub>2g</sub><sup>1</sup> (Γ) and out-of-plane mode A<sub>1g</sub><sup>1</sup> (Γ) at 1000 °C is 63.8 cm<sup>-1</sup> for the SiO<sub>2</sub>/Si substrate and 61.2 cm<sup>-1</sup> for the sapphire substrate. Both the intensity ratio of 2LA (M)/A<sub>1g</sub><sup>1</sup> (Γ) and Raman peaks difference (A<sub>1g</sub><sup>1</sup> (Γ) - E<sub>2g</sub><sup>1</sup> (Γ)) indicate the few-layer nature of the measured WS<sub>2</sub> films on both substrates similar to what has been reported in the literature<sup>33,34</sup>.

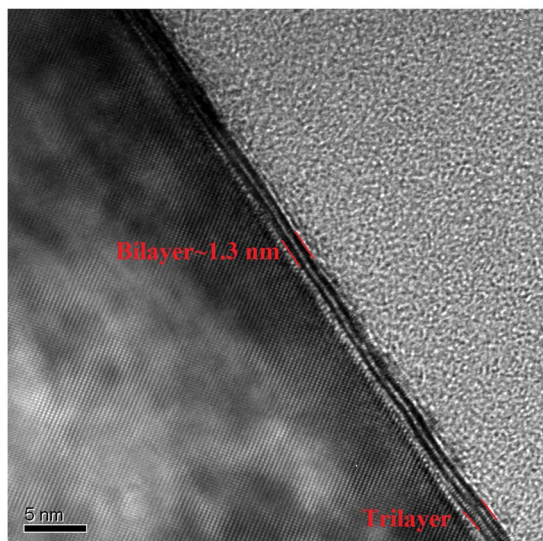


**Figure 3.** TEM image of few-layer WS<sub>2</sub> films grown on sapphire substrate. The crystalline Al<sub>2</sub>O<sub>3</sub> atomic lattice is clearly visible on the left hand side of the image. The WS<sub>2</sub> film is viewed at a high angle where bilayer and trilayer regions are also highly visible and are indicated. The bright area on the right hand side is the protective carbon coating. The trilayer region also shows the WS<sub>2</sub> atomic arrangement.

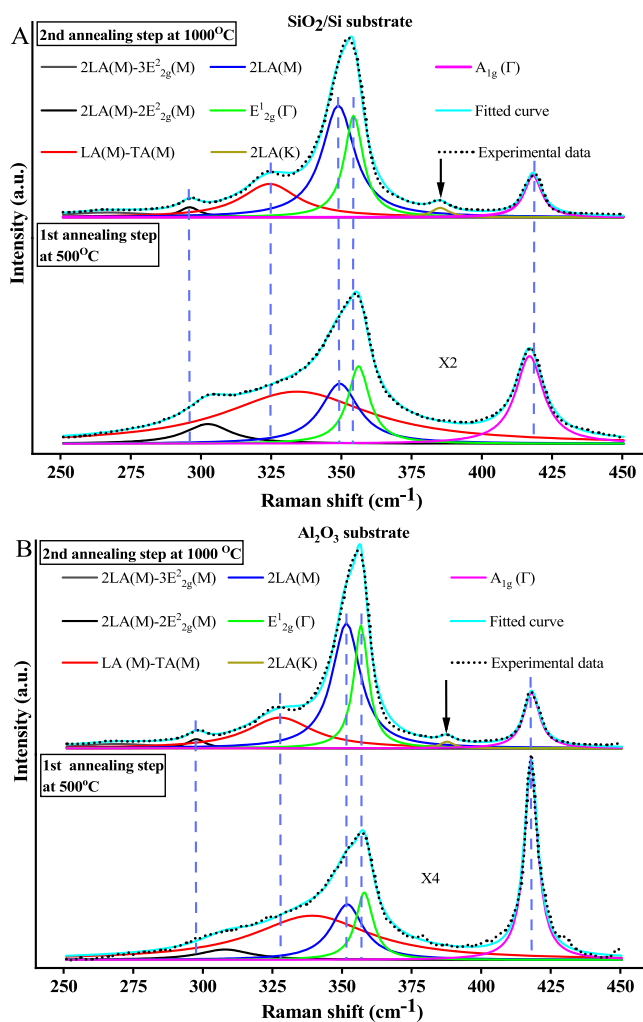


**Figure 4.** Raman spectra of WS<sub>2</sub> films on (A) SiO<sub>2</sub>/Si and (B) Sapphire at the 500 °C and 1000 °C respectively.

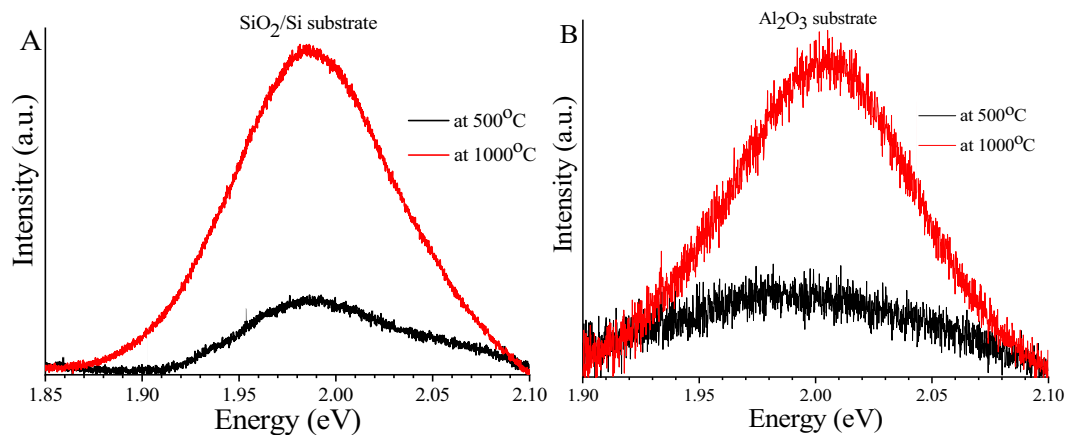


**Figure 5.** PL spectra of WS<sub>2</sub> films on (A) SiO<sub>2</sub>/Si and (B) Sapphire at 500 °C and 1000 °C respectively.

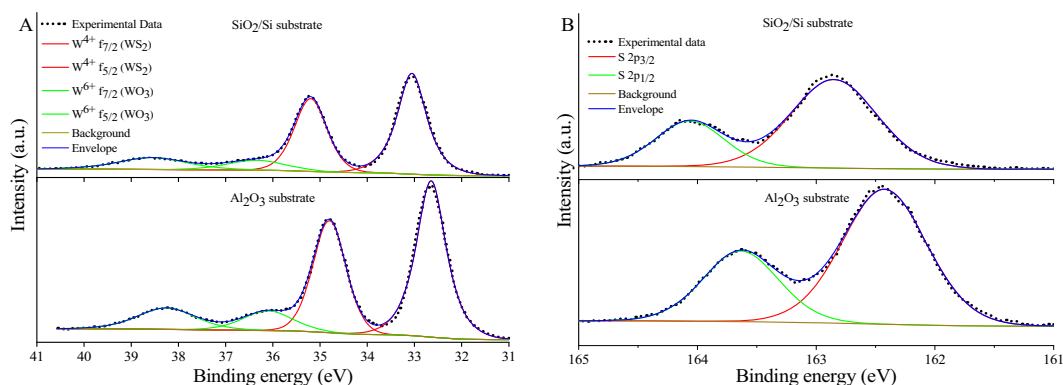


**Figure 6.** XPS spectra of WS<sub>2</sub> films on SiO<sub>2</sub>/Si and sapphire substrates (A) W 4f core-level and (B) S 2p core-level spectra.

Interestingly, after the second annealing step all the peaks from  $E_{2g}^1$  ( $\Gamma$ ) to  $2LA$  ( $M$ )- $2E_{2g}^2$  ( $M$ ) are shifted to lower wavenumbers compared to their peak positions after the first annealing step at 500 °C. The only exception was the longitudinal acoustic mode  $2LA$  ( $M$ ), which did not shift after the two annealing steps for both substrates. As a result, the separation of the in-plane  $E_{2g}^1$  ( $\Gamma$ ) and the out-of-plane peak  $A_{1g}$  ( $\Gamma$ ) Raman peaks after the first annealing step is smaller compared to after the high temperature annealing step ( $60.8\text{ cm}^{-1}$  for SiO<sub>2</sub>/Si and  $59.9\text{ cm}^{-1}$  for sapphire). This is due to blue shifts that  $E_{2g}^1$  ( $\Gamma$ ) peaks experience in poor crystalline films as stated previously. However, the intensity ratio of  $2LA$  ( $M$ )/ $A_{1g}$  ( $\Gamma$ ) peaks is also low (0.685 for the SiO<sub>2</sub>/Si and 0.285 for the sapphire) for poor crystalline films. Thus, the layer number estimation of poor crystalline WS<sub>2</sub> films (500 °C) using Raman spectra with 532 nm excitation wavelength might be not accurate. The reason behind this is the correlation between Raman peaks difference and the intensity ratio is not valid for poor crystalline WS<sub>2</sub> films (500 °C) as opposed to the higher crystalline WS<sub>2</sub> films (1000 °C) which show a clear correlation between Raman peak difference and intensity ratio when resonant excitation wavelength is used for Raman spectroscopy<sup>33</sup>.

The PL spectrum of WS<sub>2</sub> films was investigated using the same excitation wavelength, power and objective parameters as the Raman measurements. As shown in Fig. 5 there is a significant enhancement of the photoluminescence (PL) signal after high temperature annealing for both substrates. The PL intensity enhancement is X4.5 for the SiO<sub>2</sub>/Si and X3.5 for the sapphire substrate and this enhancement is attributed to the improvement in film crystallinity. However, the PL peaks intensities are still weak, due to few-layer nature of films. For the SiO<sub>2</sub>/Si substrate, the PL peak of WS<sub>2</sub> film is located at 1.984 eV, in agreement with earlier reports for few-layer WS<sub>2</sub><sup>31</sup>, whereas the PL peak position of WS<sub>2</sub> film grown on sapphire substrate is at 2 eV similar to what has been observed before for WS<sub>2</sub> films grown on sapphire<sup>35</sup>. The trivial shift to lower energy in PL peak position of the WS<sub>2</sub> films grown on SiO<sub>2</sub>/Si substrate compared to the films grown on sapphire might results from higher strain on the film deposited on SiO<sub>2</sub>/Si substrate<sup>32</sup>.

The composition of the deposited WS<sub>2</sub> films was investigated by high resolution XPS for both substrates where the W and S core levels were studied. The carbon peak in the C1s core level was used as a reference point and was at 284.8 eV for both substrates. The de-convoluted XPS spectra for W and S core levels are shown in Fig. 6(A,B) respectively for both substrates. For the WS<sub>2</sub> film deposited on the SiO<sub>2</sub>/Si substrate, two doublets were pronounced in the W core level, the first doublet represents the  $W^{4+} f_{7/2}$  at 33.05 eV and  $W^{4+} f_{5/2}$  at 35.20 eV which is attributed to WS<sub>2</sub> formation, with spin orbit splitting ( $W^{4+} f_{5/2}$ - $W^{4+} f_{7/2}$ ) of 2.15 eV and an area ratio of  $W^{4+}$

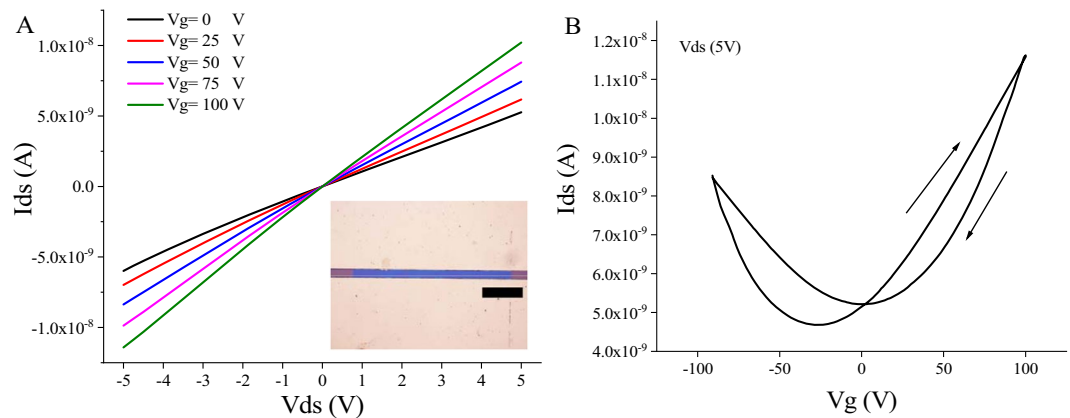


**Figure 7.** Electrical characteristics of back-gated WS<sub>2</sub> FET (A)  $I_{ds}$ - $V_{ds}$  (inset: optical microscope image for the actual FET device, the scale is 50  $\mu\text{m}$ ). (B) Forward and backward sweep transfer characteristics.

$f_{4_{5/2}}/W^{4+} f_{4_{7/2}}$  0.73. The energy of these peaks corresponds to the 2H phase of WS<sub>2</sub><sup>36</sup>. The second doublet is located at 36.35 and 38.55 eV respectively and represents the  $W^{6+} f_{4_{7/2}}$  and  $W^{6+} f_{4_{5/2}}$  peaks that depicts the formation of WO<sub>3</sub><sup>37</sup>. For sulphur, the S 2p<sub>3/2</sub> and S 2p<sub>1/2</sub> peaks are located at 162.85 and 164.06 eV respectively with spin orbit splitting (S 2p<sub>1/2</sub>-S 2p<sub>3/2</sub>) 1.21 eV and area ratio S 2p<sub>1/2</sub>/S 2p<sub>3/2</sub> 0.4. This doublet corresponds to S<sup>2-</sup> sulphur bonded in 2H phase of WS<sub>2</sub><sup>36</sup>. Fortunately, the absence of S<sub>2</sub><sup>2-</sup> ligands peaks, which corresponds to the presence of WS<sub>3</sub> and oxidized sulphur species, is a good indicator that the film is stoichiometric for both substrates<sup>37,38</sup>. The peaks obtained from the WS<sub>2</sub> films on the sapphire are almost identical to films grown on SiO<sub>2</sub>/Si. However, there is a shift to lower energies by 0.4 eV for all peaks assigned to WS<sub>2</sub> in both W and S core levels and the oxide content is negligibly increased compared to films grown on SiO<sub>2</sub>/Si.

To probe the electronic properties of the WS<sub>2</sub> film, we fabricated a back-gated field effect transistor (FET) using the as-deposited WS<sub>2</sub> films on 300 nm thermally grown SiO<sub>2</sub> on n-type Si substrates (see Fig. S5 for SEM image of the device). Indium was chosen to make direct contact with WS<sub>2</sub> due to small Schottky barrier which makes it a good choice for ohmic contacts with WS<sub>2</sub> film<sup>39</sup>. Current voltage measurements were performed in air to evaluate the transfer characteristics of the devices. First, we measured the source-drain current  $I_{ds}$  against the voltage between the source and drain  $V_{ds}$  for different bottom gate voltages as shown in Fig. 7(A), the linearity of this result reveals that the In/Au electrodes make excellent Ohmic contacts with the WS<sub>2</sub> channel. To evaluate the transconductance of the device, the back-gate voltage was swept from -91 V to 100 V in both directions as shown in Fig. 7(B). In forward sweep, the device shows n-type behaviour with  $6.2 \times 10^{-5} \text{ cm}^2/\text{V}\cdot\text{s}$  field effect mobility, a threshold voltage of -54 V and on/off ratio of 2.5. The field effect mobility was extracted from the slope of the linear part of the transfer curve using the equation:<sup>15</sup>

$$\mu_{FE} = \frac{L}{WC_{OX}V_{ds}} \frac{\Delta I}{\Delta V_g} \quad (1)$$

Where  $\mu_{FE}$  is the field effect mobility, L is the channel length (10  $\mu\text{m}$ ), W is the channel width (200  $\mu\text{m}$ ),  $C_{ox}$  is the capacitance per unit area of silicon dioxide layer (300 nm) which is (11.5 nF/cm<sup>2</sup>),  $V_{ds}$  is the source-drain voltage and  $(\Delta I/\Delta V_g)$  is the transconductance. Interestingly, in backward sweep the FET shows asymmetric ambipolar behaviour with minimum conductivity at 0 V in the n-type branch. However, the low mobility, on-off ratio and the change of the behaviour could be partially attributed to adsorbates from ambient and/or dopants that occur during photolithography and lift-off process. The field effect mobility and the on-off ratio of our WS<sub>2</sub> FET devices are comparable with backgated WS<sub>2</sub> FET devices grown by other solution-based approach when they were characterized in air<sup>40</sup>. Additionally, our WS<sub>2</sub> FET devices show comparable performance with MoS<sub>2</sub> FET devices fabricated using identical synthesis processes, where the mobility of MoS<sub>2</sub> devices varied from 10<sup>-4</sup> to 10<sup>-2</sup> cm<sup>2</sup>/V.s although the back-gate voltage of these devices was swept to much higher voltages<sup>11,15</sup>. The device field effect characteristics are dictated by the nanocrystalline nature of the film as well as ambient adsorbates. However, as it has been shown with MoS<sub>2</sub> films that are grown in similar ways, we expect a dramatic improvement when the device is optimized and operated in a top-gate configuration with a high-k dielectric such as HfO<sub>2</sub><sup>13</sup> or ionic liquid gate<sup>14,18</sup>.

## Conclusions

In conclusion, we propose a facile and cost-effective growth method that can produce high quality, continuous and ultra-thin WS<sub>2</sub> films for electronic applications. This solution-based method utilizes thermal decomposition of uniform spin coated ammonium tetrathiotungstate films on two different types of substrates with centimetre scale to create thin WS<sub>2</sub> films. The key factor that enables (NH<sub>4</sub>)<sub>2</sub>WS<sub>4</sub> to successfully form a uniform and continuous film is our optimized solvents recipe with volume ratio 3/6 NMP, 2/6 n-butylamine and 1/6 2-aminoethanol that promotes the solubility and wettability of the precursor solution. Different characterization tools were used to confirm the thickness and the quality of the WS<sub>2</sub> films. Finally, we demonstrated for the first time a back-gated

FET from an as-deposited WS<sub>2</sub> film grown by our solution based process with an electron mobility reaching  $6.2 \times 10^{-5} \text{ cm}^2/\text{V.s}$  which shows comparable performance to MoS<sub>2</sub> devices fabricated by similar synthesis approaches.

## Materials and Methods

**Preparation of the substrates and (NH<sub>4</sub>)<sub>2</sub>WS<sub>4</sub> solutions for growth of WS<sub>2</sub> films.** We used  $1.5 \times 1.5 \text{ cm}^2$  SiO<sub>2</sub>/Si (300 nm SiO<sub>2</sub>) and sapphire substrates to assess the optimum spin coating conditions for different solvent solutions. Prior to spin coating, the surface of the substrates was cleaned using acetone, isopropanol and de-ionized water followed by conditioning using oxygen plasma at 0.1 mb pressure (oxygen flow 1000 mL/min) and 1000 W power for 15 min to enhance the wettability. To prepare the solutions, we dissolved 174 mg of (NH<sub>4</sub>)<sub>2</sub>WS<sub>4</sub> in 5 mL of each solvent (DMF, ethylene glycol, NMP) to form 100 mM of precursor solution. After one hour of sonication (at 70 °C) the three solutions were spin coated on the substrates at three different speeds (3000, 6000 and 9000 rpm) for 1 min (step 1: ramp 5 sec, dwell time 5 sec, rpm 500; step 2: ramp 5 sec, dwell time 45 sec, rpm 3000, 6000 and 9000). After spinning, the substrates were prebaked at 140 °C for 1 min using a hot-plate where the solvents evaporated. Prior to thermal decomposition, the refined recipe for the new solvents system we propose (6 mL total volume) is 3/6 NMP, 2/6 butylamine and 1/6 2-aminoethanol. We mixed these solvents together and dissolved (208, 73, 42 and 21) mg of (NH<sub>4</sub>)<sub>2</sub>WS<sub>4</sub> to create solutions of (100, 35, 20, 10) mM. The solutions were then sonicated for 1 hour at 70 °C before being spin coated at 6000 rpm (the same spin-coating recipe was used as before) on the cleaned and oxygen plasma treated substrates (the same oxygen plasma recipe was used as before). Finally, the samples were baked on a hot-plate at 140 °C for 1 minute.

**Thermal decomposition.** The 35 mM concentration samples were used for the thermal decomposition. They were placed in a tube furnace and purged with a 6% H<sub>2</sub> in Ar gas at 8 mb pressure for 5 minutes. The samples were kept in the cold zone and the furnace was programmed to reach 500 °C. After 20 minutes of temperature stabilization, the samples were moved in the hot zone of the furnace. After 30 min of annealing at 500 °C, the samples were removed from the furnace and were left to cool down naturally while maintaining the flow of gas. To improve the crystallinity of our films we performed a second annealing step at 1000 °C. The samples with identical substrates were arranged in film-facing pairs to prevent the reduction of the films (see Fig. S6). Firstly, the furnace tube was purged with Argon at a pressure of 1 mb for 5 minutes to remove oxygen from the system. The system was then allowed to reach atmospheric pressure under the same 100 sccm Ar flow. After a 40 min temperature ramp, the furnace reached 1000 °C to anneal the samples for 15 minutes before removal from the hot zone to let the samples cool down to room temperature under the same gas and pressure conditions. See Fig. S7 for optical microscopy image of the final WS<sub>2</sub> film grown on SiO<sub>2</sub>/Si.

**Device fabrication.** The transistor channels were formed by conventional photolithography using S1813 photoresist masking and etched for 2 minutes to remove unwanted WS<sub>2</sub> film regions by Argon ion milling using Oxford Plasma Technology Ionfab 300 plus system. An Argon ion plasma beam was accelerated to 500 V with 100 mA current. The sample placed on a cooled plate (15 °C) at an angle of 45° with respect to the beam and rotated at 5 rpm. The samples were then immersed in acetone to remove the photoresist mask and obtain a WS<sub>2</sub> channel of 200 μm width which represents the FET. The length of the channel is 10 μm and was defined by the source and drain electrodes positions as patterned by S1805 photoresist. Indium contacts (10 nm thick) were deposited and capped by 50 nm of Au using an e-beam evaporator followed by lift-off.

**Characterization.** AFM images were produced using an Agilent 5500 scanning probe microscope. Raman and PL spectroscopy were conducted using Invia Raman Microscope (Renishaw) system with a 532 nm excitation wavelength at 20 mW power and 50X objective. XPS has been performed using a Thermo fisher scientific Thetaprobe system. SEM was performed using a Joel JSM-7500F FEG-SEM. The preparation of the lamella was performed using a Zeiss NVision 40 CrossBeam FIB system. TEM was performed in the Loughborough Materials Characterisation Centre using an FEI Tecnai F20. Electrical measurements were performed in air using an Agilent 4155C semiconductor parameter analyser connected to a cascade micropositioning stage.

Received: 16 April 2019; Accepted: 14 January 2020;

Published online: 03 February 2020

## References

1. Fiori, G. *et al.* Electronics based on two-dimensional materials. *Nat. Nanotechnol.* **9**, 768–779 (2014).
2. Chhowalla, M. *et al.* The chemistry of two-dimensional layered transition metal dichalcogenide nanosheets. *Nat. Chem.* **5**, 263–275 (2013).
3. Mak, K. F., Lee, C., Hone, J., Shan, J. & Heinz, T. F. Atomically thin MoS<sub>2</sub>: A new direct-gap semiconductor. *Phys. Rev. Lett.* **105**, 136805 (2010).
4. Splendiani, A. *et al.* Emerging photoluminescence in monolayer MoS<sub>2</sub>. *Nano Lett.* **10**, 1271–1275 (2010).
5. Mak, K. F., McGill, K. L., Park, J. & McEuen, P. L. Valleytronics. The valley Hall effect in MoS<sub>2</sub> transistors. *Science* **344**, 1489–92 (2014).
6. Radisavljevic, B., Radenovic, A., Brivio, J., Giacometti, V. & Kis, A. Single-layer MoS<sub>2</sub> transistors. *Nat. Nanotechnol.* **6**, 147–150 (2011).
7. Coleman, J. N. *et al.* Two-dimensional nanosheets produced by liquid exfoliation of layered materials. *Science* **331**, 568–71 (2011).
8. Tan, L. K. *et al.* Atomic layer deposition of a MoS<sub>2</sub> film. *Nanoscale* **6**, 10584–10588 (2014).
9. Amani, M. *et al.* High Luminescence Efficiency in MoS<sub>2</sub> Grown by Chemical Vapor Deposition. *ACS Nano* **10**, 6535–6541 (2016).
10. Samadi, M. *et al.* Group 6 transition metal dichalcogenide nanomaterials: Synthesis, applications and future perspectives. *Nanoscale Horizons* **3**, 90–204 (2018).
11. Liu, K.-K. *et al.* Growth of Large-Area and Highly Crystalline MoS<sub>2</sub> Thin Layers on Insulating Substrates. *Nano Lett.* **12**, 1538–1544 (2012).

12. George, A. S. *et al.* Wafer Scale Synthesis and High Resolution Structural Characterization of Atomically Thin MoS<sub>2</sub> Layers. *Adv. Funct. Mater.* **24**, 7461–7466 (2014).
13. Yang, J. *et al.* Wafer-scale synthesis of thickness-controllable MoS<sub>2</sub> films via solution-processing using a dimethylformamide/n-butylamine/2-aminoethanol solvent system. *Nanoscale* **7**, 9311–9319 (2015).
14. Lim, Y. R. *et al.* Wafer-Scale, Homogeneous MoS<sub>2</sub> Layers on Plastic Substrates for Flexible Visible-Light Photodetectors. *Adv. Mater.* **28**, 5025–5030 (2016).
15. Hung, Y. H. *et al.* Scalable Patterning of MoS<sub>2</sub> Nanoribbons by Micromolding in Capillaries. *ACS Appl. Mater. Interfaces* **8**, 20993–21001 (2016).
16. Ionescu, R. *et al.* Chelant Enhanced Solution Processing for Wafer Scale Synthesis of Transition Metal Dichalcogenide Thin Films. *Sci. Rep.* **7**, 6419 (2017).
17. Yang, H. *et al.* Highly Scalable Synthesis of MoS<sub>2</sub> Thin Films with Precise Thickness Control via Polymer-Assisted Deposition. *Chem. Mater.* **29**, 5772–5776 (2017).
18. Lim, Y. R. *et al.* Roll-to-Roll Production of Layer-Controlled Molybdenum Disulfide: A Platform for 2D Semiconductor-Based Industrial Applications. *Adv. Mater.* **30**, 1705270 (2018).
19. Zhao, W. *et al.* Evolution of Electronic Structure in Atomically Thin Sheets of WS<sub>2</sub> and WSe<sub>2</sub>. *ACS Nano* **7**, 791–797 (2013).
20. Liu, L., Kumar, S. B., Ouyang, Y. & Guo, J. Performance limits of monolayer transition metal dichalcogenide transistors. *IEEE Trans. Electron Devices* **58**, 3042–3047 (2011).
21. Hwang, W. S. *et al.* Transistors with chemically synthesized layered semiconductor WS<sub>2</sub> exhibiting 10<sup>5</sup> room temperature modulation and ambipolar behavior. *Appl. Phys. Lett.* **101**, 013107 (2012).
22. Orofeo, C. M., Suzuki, S., Sekine, Y. & Hibino, H. Scalable synthesis of layer-controlled WS<sub>2</sub> and MoS<sub>2</sub> sheets by sulfurization of thin metal films. *Appl. Phys. Lett.* **105**, 83112 (2014).
23. Gutiérrez, H. R. *et al.* Extraordinary room-temperature photoluminescence in triangular WS<sub>2</sub> monolayers. *Nano Lett.* **13**, 3447–3454 (2013).
24. Kwon, K. C. *et al.* Tungsten disulfide thin film/p-type Si heterojunction photocathode for efficient photochemical hydrogen production. *MRS Commun.* **7**, 272–279 (2017).
25. Li, Z. *et al.* Facile synthesis of large-area and highly crystalline WS<sub>2</sub> film on dielectric surfaces for SERS. *J. Alloys Compd.* **666**, 412–418 (2016).
26. Kwon, K. C. *et al.* Synthesis of atomically thin transition metal disulfides for charge transport layers in optoelectronic devices. *ACS Nano* **9**, 4146–4155 (2015).
27. Annamalai, M. *et al.* Surface energy and wettability of van der Waals structures. *Nanoscale* **8**, 5764–5770 (2016).
28. Srinivasan, B. R., Näther, C., Dhuri, S. N. & Bensch, W. On the importance of H-bonding interactions in organic ammonium tetrathiotungstates. *Monatshfte für Chemie* **137**, 397–411 (2006).
29. Srinivasan, B. R., Naik, A. R., Näther, C. & Bensch, W. Synthesis, spectroscopy and crystal structures of chiral organic ammonium tetrathiometalates showing N-H...S and C-H...S interactions. *Zeitschrift für Anorg. und Allg. Chemie* **633**, 582–588 (2007).
30. Zhao, W. *et al.* Lattice dynamics in mono- and few-layer sheets of WS<sub>2</sub> and WSe<sub>2</sub>. *Nanoscale* **5**, 9677–9683 (2013).
31. Bissett, M. A., Hattle, A. G., Marsden, A. J., Kinloch, I. A. & Dryfe, R. A. W. Enhanced Photoluminescence of Solution-Exfoliated Transition Metal Dichalcogenides by Laser Etching. *ACS Omega* **2**, 738–745 (2017).
32. Su, L., Yu, Y., Cao, L. & Zhang, Y. Effects of substrate type and material-substrate bonding on high-temperature behavior of monolayer WS<sub>2</sub>. *Nano Res.* **8**, 2686–2697 (2015).
33. Berkdemir, A. *et al.* Identification of individual and few layers of WS<sub>2</sub> using Raman Spectroscopy. *Sci. Rep.* **3**, 1755 (2013).
34. Li, D. H. *et al.* Dielectric functions and critical points of crystalline WS<sub>2</sub> ultrathin films with tunable thickness. *Phys. Chem. Chem. Phys.* **19**, 12022–12031 (2017).
35. Lan, F. *et al.* Synthesis of large-scale single-crystalline monolayer WS<sub>2</sub> using a semi-sealed method. *Nanomaterials* **8**, 100 (2018).
36. Sang, Y. *et al.* From UV to near-infrared, WS<sub>2</sub> nanosheet: A novel photocatalyst for full solar light spectrum photodegradation. *Adv. Mater.* **27**, 363–369 (2015).
37. Tan, S. M. & Pumera, M. Bottom-up Electrosynthesis of Highly Active Tungsten Sulfide (WS<sub>3-x</sub>) Films for Hydrogen Evolution. *ACS Appl. Mater. Interfaces* **8**, 3948–3957 (2016).
38. Alsabban, M. M. *et al.* Editors' Choice Growth of Layered WS<sub>2</sub> Electrocatalysts for Highly Efficient Hydrogen Production Reaction. *ECS J. Solid State Sci. Technol.* **5**, Q3067–Q3071 (2016).
39. Wang, Y. *et al.* Van der Waals contacts between three-dimensional metals and two-dimensional semiconductors. *Nature* **568**, 70–74 (2019).
40. Lan, C., Li, C., Yin, Y. & Liu, Y. Large-area synthesis of monolayer WS<sub>2</sub> and its ambient-sensitive photo-detecting performance. *Nanoscale* **7**, 5974–5980 (2015).

## Acknowledgements

The first author gratefully acknowledge the financial support from The Higher Committee for Education Development in Iraq (HCED Iraq). The authors acknowledge financial support from the UK's Engineering and Physical Sciences Council through National Hub in High Value Photonic Manufacturing (grant EP/N00762X/1).

## Author contributions

O.A.A., S.M. and P.S. conceived the idea. O.A.A. and I.Z. composed the manuscript. O.A.A. designed the experiments, synthesised the films, fabricated and characterised the FET device. H.W. performed the AFM and the XPS characterisations under supervision of C.C.H. A.H.L. performed the Raman and Photoluminescence spectroscopy. N.P.S. helped with fabrication of the device. I.Z. and N.A. analysed the XPS data. I.Z. performed the SEM. M.E. prepared the TEM lamella. The whole work was supervised and managed by D.H., S.M. and P.S.

## Competing interests

The authors declare no competing interests.

## Additional information

**Supplementary information** is available for this paper at <https://doi.org/10.1038/s41598-020-58694-0>.

**Correspondence** and requests for materials should be addressed to P.S.

**Reprints and permissions information** is available at [www.nature.com/reprints](http://www.nature.com/reprints).

**Publisher's note** Springer Nature remains neutral with regard to jurisdictional claims in published maps and institutional affiliations.



**Open Access** This article is licensed under a Creative Commons Attribution 4.0 International License, which permits use, sharing, adaptation, distribution and reproduction in any medium or format, as long as you give appropriate credit to the original author(s) and the source, provide a link to the Creative Commons license, and indicate if changes were made. The images or other third party material in this article are included in the article's Creative Commons license, unless indicated otherwise in a credit line to the material. If material is not included in the article's Creative Commons license and your intended use is not permitted by statutory regulation or exceeds the permitted use, you will need to obtain permission directly from the copyright holder. To view a copy of this license, visit <http://creativecommons.org/licenses/by/4.0/>.

© The Author(s) 2020